ECCOMAS Congress 2016
VII European Congress on Computational Methods in Applied Sciences and Engineering
M. Papadrakakis, V. Papadopoulos, G. Stefanou, V. Plevris (eds.)
Crete Island, Greece, 5–10 June 2016

THERMO-ELASTICITY IN SHELL STRUCTURES MADE OF FUNCTIONALLY GRADED MATERIALS (ECCOMAS CONGRESS 2016)

Stephan Kugler[1], Peter A. Fotiu[1], and Justin Murin[2]

[1]Department of Applied and Numerical Mechanics,
University of Applied Sciences Wiener Neustadt,
Johannes Gutenbergstraße 3, Wiener Neustadt, Austria
e-mail: {kugler,fotiu}@fhwn.ac.at

[2] Department of Applied Mechanics and Mechatronics,
Institute for Automotive Mechatronics,
Faculty of Electrical Engineering and Information Technology,
Slovak University of Technology in Bratislava, Slovakia
Ilkovicova 3, 81219 Bratislava, Slovakia
e-mail: justin.murin@stuba.sk

Keywords: Thermo-Elasticity, FGM-Shell-Structures, Drilling degrees of freedom, Two-Step-Algorithm.

Abstract. *An efficient low order finite shell element is derived for the thermo-elastic analysis of shell structures made of functionally graded materials or multilayer composites. It is based on a one-way coupling between the thermal and the mechanical analysis. The thermal quantities are evaluated using a new iterative scheme that properly accounts for convection boundary conditions and large gradients of the thermal conductivity. The resulting non-constant temperature field with respect to the thickness direction gives nodal forces and couples, which are applied on a shear weak six parameter shell formulation. Here, drill rotations are included, supplemented with a proper method for calculating effective elastic properties. Numerical results indicate efficiency and accuracy of the proposed approach.*

1 Introduction

This paper focuses on the analysis of thermo-elastic effects in shell structures of functionally graded materials (FGM) or multilayer composites (MLC). The constitutive model is characterized by a variation of material properties, which is continuous in FGMs and discontinuous in MLCs. We focus only on arbitrary variations in transverse direction. Variations with respect to the membrane directions can be modeled easily using a discretization scheme with elements each showing constant transverse variations. FGM and MLC structures play an important role in the development of sensors and actuators (see [1] and references therein) and accurate virtual analysis procedures are required.

Many papers deal with the static and dynamic analysis of FGM beams with transverse variations of material properties. In [2] elasticity solutions for simply supported FGM beams are given using the Euler-Bernoulli beam theory. Chakraborty et al. [3] discuss thermo-elastic beam problems based on the first order shear theory. Mahi et al. [4] consider free vibrations of symmetric FGM beams subjected to an initial thermal stress. In case of combined variations of material properties in transverse and longitudinal directions, many achievements are due to Murin et al. [5, 6, 7]. The amount of literature dealing with FGM shells is also overwhelming. In Shen [8] special attention is put onto the nonlinear response of FGM plates. In [9, 10] electro-mechanical analyses of FGM shells with piezo-electric layers are proposed. Thermo-elastic analysis procedures of FGM plate and shell structures are discussed in [11]. There, a higher order shell formulation is used. However, only little literature is found if drill rotations (i.e. the rotation about the shell's normal) are to be included. This frequently missing sixth nodal degree of freedom gets important if shell structures are combined with beam structures. There, any torsional moment within the beam directly activates drill rotations if the beam axis is perpendicular to the shell's membrane. In that field many achievements are due to Kugler et al. [12, 13], where references to earlier procedures [14] can be found. A generalization of those procedures to FGMs and MLCs are given in [15, 16] where elasticity is described using effective elastic properties derived in [15].

In this paper we discuss a numerical framework to analyze thermo-elastic effects in FGM and MLC shells. Frequently, the variation of Poisson's ratio in FGMs and MLCs does not show large gradients - therefore, we assume Poisson's ratio to be constant. As boundary conditions we consider the following cases:

- Nodal temperatures (Dirichlet-type): The mean temperature at any node is prescribed.
- Convection on top- and bottom-surface (von Neumann-type): Convection is applied independently onto the top- and bottom-surface prescribing the gradient of the non-constant transverse temperature distribution.
- Nodal displacements and rotations (Dirichlet-type): Displacements and rotations are prescribed.
- Mechanical loads (von Neumann-type): Any transverse and in-plane mechanical loads can be applied onto the finite element model.

The present paper is organized as follows: In Sect. 2 the details of the proposed numerical framework is discussed. We start with describing the thermal analyses in Sect. 2.1. The temperature field in FGM and MLC shells is found for an arbitrary variation of thermal conductivity and convection conditions. Non-constant temperature distributions with respect to the thickness

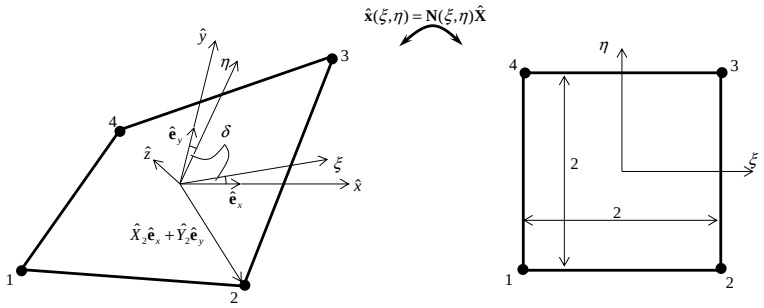

Figure 1: Plane quadrilateral with skew angled element coordinates ξ and η

direction require an iterative solution scheme. The mechanical analysis is discussed in Sect. 2.2. There, a quadrilateral six parameter shell element is described, where drilling rotations are included within the membrane part of the stiffness matrix. The bending part of the stiffness matrix incorporates a shear elastic behavior with an exact thin plate limit. A projection procedure for arbitrarily warped element geometries is included. Arbitrary variations of the Young's modulus require four effective elastic properties, i.e. the offset of a mechanical neutral surface from the discretized mid-surface, effective moduli for membrane and bending properties and a shear correction factor. In Sect. 2.3 an efficient one-way coupling scheme between the thermal and the mechanical field is proposed. Based on the evaluated temperature distributions internal nodal forces and couples are calculated, which are applied onto the mechanical model. The numerical accuracy and the effectiveness of the proposed formulation is discussed in Sect. 3. There, solutions based on the proposed framework are compared to continuum solutions found with ANSYS an to reference solutions found in literature. Finally, in Sect. 4 conclusions are drawn.

2 Numerical procedure

Consider a curved FGM or MLC shell geometry of thickness h, where the geometrical mid-surface is discretized by four noded shell elements. Thus, the element configuration could possibly be warped. Any warped surface geometries do not pose a problem if scalar fields like temperature distributions are analyzed (see Sect. 2.1). However, in mechanical analyses warped shell elements lead to a coupling between membrane and bending properties, which can be circumvented by special projection schemes (see Sect. 2.2). Within each element we assume material properties to be constant in membrane directions $\hat{x}$ - $\hat{y}$ and variable in transverse direction $\hat{z}$.

Since both the thermal analysis and the mechanical analysis is based on a four noded finite element, we introduce a two dimensional element kinematics. The nodal coordinates of the i-th node ($i = 1, 2, 3, 4$) read $\hat{\mathbf{r}}_i = \hat{X}_i\hat{\mathbf{e}}_x + \hat{Y}_i\hat{\mathbf{e}}_y$ and the mapping (Fig. 1) between the Cartesian and the parameter coordinates is carried out using the classical bilinear shape functions [17],

$$\begin{bmatrix} \hat{x} \\ \hat{y} \end{bmatrix} = \begin{bmatrix} \mathbf{N} & \mathbf{0} \\ \mathbf{0} & \mathbf{N} \end{bmatrix} \begin{bmatrix} \hat{\mathbf{X}} \\ \hat{\mathbf{Y}} \end{bmatrix} \tag{1}$$

with

$$\mathbf{N} = \begin{bmatrix} N_1 & N_2 & N_3 & N_4 \end{bmatrix}$$

$$N_1 = \frac{1}{4}(1-\xi)(1-\eta) \quad , \quad N_2 = \frac{1}{4}(1+\xi)(1-\eta) \ ,$$

$$N_3 = \frac{1}{4}(1+\xi)(1+\eta) \quad , \quad N_4 = \frac{1}{4}(1-\xi)(1+\eta) \ . \tag{2}$$

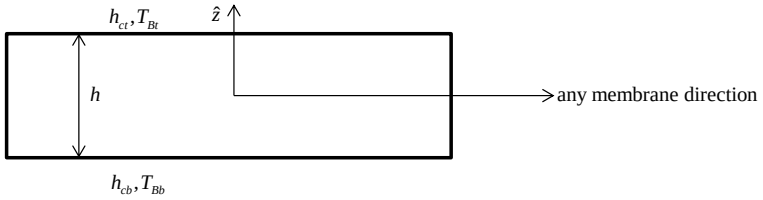

Figure 2: Description of the thermal field problem

In (1) the nodal coordinates are arranged as $\hat{\mathbf{X}} = \left[\begin{array}{cccc} \hat{X}_1 & \hat{X}_2 & \hat{X}_3 & \hat{X}_4 \end{array} \right]^T$ and $\hat{\mathbf{Y}} = \left[\begin{array}{cccc} \hat{Y}_1 & \hat{Y}_2 & \hat{Y}_3 & \hat{Y}_4 \end{array} \right]^T$. An alternative formulation [18] of the shape functions (2) is

$$\mathbf{N} = \boldsymbol{\Delta} + \mathbf{b}_x \hat{x} + \mathbf{b}_y \hat{y} + \boldsymbol{\gamma} \xi \eta, \tag{3}$$

with

$$\mathbf{b}_x = \frac{1}{2A_e} \left[\begin{array}{cccc} \hat{y}_{24} & \hat{y}_{31} & \hat{y}_{42} & \hat{y}_{13} \end{array} \right] , \; \mathbf{b}_y = \frac{1}{2A_e} \left[\begin{array}{cccc} \hat{x}_{42} & \hat{x}_{13} & \hat{x}_{24} & \hat{x}_{31} \end{array} \right] , \tag{4}$$

$$\boldsymbol{\gamma} = \frac{1}{4A_e} \left[\begin{array}{c} \hat{X}_2 \hat{y}_{34} + \hat{X}_3 \hat{y}_{42} + \hat{X}_4 \hat{y}_{23} \\ \hat{X}_1 \hat{y}_{43} + \hat{X}_3 \hat{y}_{14} + \hat{X}_4 \hat{y}_{31} \\ \hat{X}_1 \hat{y}_{24} + \hat{X}_2 \hat{y}_{41} + \hat{X}_4 \hat{y}_{12} \\ \hat{X}_1 \hat{y}_{32} + \hat{X}_2 \hat{y}_{13} + \hat{X}_3 \hat{y}_{21} \end{array} \right]^T , \tag{5}$$

$$\boldsymbol{\Delta} = \frac{1}{4} \left[\mathbf{t} - \left(\sum_{i=1}^{4} \hat{X}_i \right) \mathbf{b}_x - \left(\sum_{i=1}^{4} \hat{Y}_i \right) \mathbf{b}_y \right] , \tag{6}$$

$$\mathbf{t} = \left[\begin{array}{cccc} 1 & 1 & 1 & 1 \end{array} \right] , \tag{7}$$

$$\hat{x}_{IJ} = \hat{X}_I - \hat{X}_J \, , \; \hat{y}_{IJ} = \hat{Y}_I - \hat{Y}_J \, , \; A_e = \frac{1}{2} \left(\hat{x}_{24} \hat{y}_{31} + \hat{x}_{31} \hat{y}_{42} \right) . \tag{8}$$

2.1 Thermal analysis

In this section we evaluate the temperature field $T(\hat{x}, \hat{y}, \hat{z})$ within the shell's volume. Consider a FGM or MLC shell structure of thickness h with a transversely varying thermal conductivity k, where convection is applied onto the outer surfaces. Figure 2 shows a cut through the shell structure, where convection is applied independently onto the top- and bottom-surface, i.e.

$$\hat{z} = -h/2 : \;\; q_n^b = h_{cb}(T(\hat{z} = -h/2) - T_{Bb}), \tag{9}$$

$$\hat{z} = h/2 : \;\; q_n^t = h_{ct}(T(\hat{z} = h/2) - T_{Bt}). \tag{10}$$

In (9) and (10) h_{ct} and h_{cb} denote the convection coefficient on the top and bottom surface, while T_{Bt} and T_{Bb} are the temperatures of the adjacent fluid. We decompose $T(\hat{x}, \hat{y}, \hat{z})$ according to

$$T(\hat{x}, \hat{y}, \hat{z}) = \bar{T}(\hat{x}, \hat{y}) + \widetilde{T}(\hat{z}), \tag{11}$$

where

$$\bar{T}(\hat{x}, \hat{y}) = 1/h \int_h T(\hat{x}, \hat{y}, \hat{z}) \, d\hat{z}, \tag{12}$$

is the mean temperature, while $\widetilde{T}(\hat{z})$ describes the unknown temperature distribution in transverse direction. The iterative solution strategy consists of two steps:

1. Evaluation of the mean temperature $\bar{T}(\hat{x},\hat{y}) = {}^1\!/_h \int_h T(\hat{x},\hat{y},\hat{z})\, d\hat{z}$ in membrane direction.
2. Estimate $\widetilde{T}(\hat{z})$ based on a mean temperature $\bar{T}$.

An iterative procedure with iteration number I is required since the shell's surface temperatures are initially unknown. Hence, (9) and (10) cannot be satisfied exactly, and we rewrite (9) and (10) according to

$$\hat{z} = -{}^h\!/_2 : \quad q_n^{b\,I+1} = h_{cb}(\bar{T}^{I+1} - T_{Bb}^{*I}),$$

$$\hat{z} = {}^h\!/_2 : \quad q_n^{t\,I+1} = h_{ct}(\bar{T}^{I+1} - T_{Bt}^{*I}), \tag{13}$$

with

$$T_{Bb}^{*I} = T_{Bb} - \widetilde{T}^I(\hat{z} = -{}^h\!/_2),$$

$$T_{Bt}^{*I} = T_{Bt} - \widetilde{T}^I(\hat{z} = {}^h\!/_2). \tag{14}$$

The **global iterative algorithm** can be summarized as follows:

1. $I = 0$
2. $\widetilde{T}^{I=0}(\hat{z} = \pm {}^h\!/_2) = 0$
3. WHILE $\frac{\bar{T}^{I+1} - \bar{T}^I}{\bar{T}^{I+1}} <$ tol (tol = tolerance limit)
   (a) $T_{Bb}^{*I} = T_{Bb} - \widetilde{T}^I(\hat{z} = -{}^h\!/_2)$ and $T_{Bt}^{*I} = T_{Bt} - \widetilde{T}^I(\hat{z} = {}^h\!/_2)$
   (b) FIND $\bar{T}^{I+1}$ according to Sect. 2.1.1 using convection boundary condition (13) and (14).
   (c) FIND $\widetilde{T}^{I+1}$ according to Sect. 2.1.2
   (d) $I = I + 1$

2.1.1 Evaluation of mean temperature

In this section we discuss a suitable procedure to evaluate the mean temperature $\bar{T}$. The strong form of the corresponding boundary value problem [19] reads

$$\bar{k}\bar{T}_{,ii} = 0, \tag{15}$$

$$\bar{T} = T_0 \ \text{ at } \ \Gamma_T, \tag{16}$$

$$q_0 = q_n = -\bar{k}\bar{T}_{,i} n_i \ \text{ at } \ \Gamma_q. \tag{17}$$

where a comma within an index denotes a partial derivative and Einstein's summation convention is understood ($i = \hat{x}, \hat{y}$). The Dirichlet boundary condition (16) prescribes a given value T_0 at the boundary Γ_T, while the von Neumann boundary condition prescribes the heat flux $q_i n_i$

along Γ_q. In (17) $-\bar{k}\bar{T}_{,i} = \bar{q}_i$ is the mean heat flux, while $\bar{k}$ denotes the mean value of thermal conductivity,

$$\bar{k} = \frac{1}{h}\int_h k(\hat{z})d\hat{z}. \tag{18}$$

The weak form of (15)-(17) is given by,

$$\int_V \bar{k}\bar{T}_{,ii}\delta\bar{T}dV - \int_{\Gamma_q}(q_0 - q_n)\delta\bar{T}d\Gamma = 0, \tag{19}$$

where the weighting function $\delta\bar{T}$ is a virtual temperature distribution that has to satisfy the Dirichlet boundary condition $\delta\bar{T} = 0$ at Γ_T. Applying the Gaussian theorem to the first integral leads to

$$\int_V \bar{k}\bar{T}_{,i}\delta\bar{T}_{,i}dV + \int_{\Gamma_q} q_0\delta\bar{T}d\Gamma = 0. \tag{20}$$

We use bilinear interpolations (2) for the mean temperature fields

$$\bar{T} = \mathbf{N}\bar{\mathbf{T}}^e \;\text{ and }\; \delta\bar{T} = \mathbf{N}\delta\bar{\mathbf{T}}^e\ , \tag{21}$$

where $\bar{\mathbf{T}}^e$ and $\delta\bar{\mathbf{T}}^e$ denote the corresponding nodal values. Introducing this into (20) yields

$$\begin{aligned}\left(\delta\bar{\mathbf{T}}^e\right)^T \Bigg[&\underbrace{\bar{k}h\int_{-1}^{1}\int_{-1}^{1}\mathbf{B}^T\mathbf{B}\det\mathbf{J}\,d\xi d\eta}_{\mathbf{K}_T^e}\bar{\mathbf{T}}^e + \\ &+\underbrace{\int_{-1}^{1}\int_{-1}^{1}\left(h_{ct}+h_{cb}\right)\mathbf{N}^T\mathbf{N}\det\mathbf{J}\,d\xi d\eta}_{\mathbf{K}_{Tc}^e}\bar{\mathbf{T}}^e - \\ &-\underbrace{\int_{-1}^{1}\int_{-1}^{1}\left(h_{ct}T_{Bt}^* + h_{cb}T_{Bb}^*\right)\mathbf{N}^T\det\mathbf{J}\,d\xi d\eta}_{\mathbf{F}_{Tc}^e}\Bigg] = 0,\end{aligned} \tag{22}$$

with $\mathbf{B}$ referring to the gradient of the shape functions,

$$\mathbf{B} = \begin{bmatrix}\mathbf{B}_{\hat{x}}\\ \mathbf{B}_{\hat{y}}\end{bmatrix} = \begin{bmatrix} N_{1,\hat{x}} & N_{2,\hat{x}} & N_{3,\hat{x}} & N_{4,\hat{x}} \\ N_{1,\hat{y}} & N_{2,\hat{y}} & N_{3,\hat{y}} & N_{4,\hat{y}}\end{bmatrix}. \tag{23}$$

We assume that $\widetilde{T}(\hat{z})$ is constant within one element, thus, T_{Bt}^* and T_{Bb}^* from (14) is also elementwise constant and is evaluated at each element's center. The differential volume of a shell structure is given by $dV = hdA = h\det\mathbf{J}\,d\xi d\eta$, where $\det\mathbf{J}$ denotes the determinant of the element Jacobian. With (22) we finally obtain

$$\left(\mathbf{K}_T^e + \mathbf{K}_{Tc}^e\right)\bar{\mathbf{T}}^e = \mathbf{F}_{Tc}^e, \tag{24}$$

Equations (24) have to be assembled to a global system in a standard manner [20]. All integrations over the element domain are carried out numerically by a 2×2 Gauss integration.

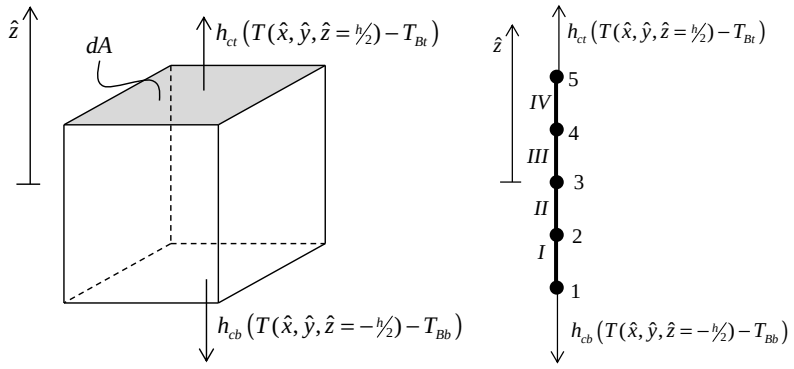

(a) Problem of transverse temperature distribution

(b) Discretized problem of transverse temperature distribution ($n = 4$)

Figure 3: Transverse temperature distribution

2.1.2 Evaluation of transverse temperature distribution

Once the mean temperature $\bar{T}(\hat{x},\hat{y})$ is evaluated at every point of the shell's structure, the temperature distribution with respect to the thickness direction is calculated. Thereby, we analyze the problem depicted in Fig. 3(a) showing an infinitesimal volume portion of cross section dA and a height of h where a convection boundary condition on the top and bottom surface is applied. In what follows we discuss a procedure where the temperature distribution with respect to the thickness direction is found from a thermal conduction problem with two Neumann conditions. At every location $\hat{x}$ and $\hat{y}$ the following system of equations holds[1]

$$\frac{d}{d\hat{z}}\left(k(\hat{x},\hat{y},\hat{z})\frac{d}{d\hat{z}}T(\hat{x},\hat{y},\hat{z})\right)+K^*=0\ , \tag{25}$$

$$\hat{z}=h/2:\ -k(\hat{x},\hat{y},\hat{z}=h/2)\left.\frac{dT(\hat{x},\hat{y},\hat{z})}{d\hat{z}}\right|_{\hat{z}=h/2}-h_{ct}\left(T(\hat{x},\hat{y},\hat{z}=h/2)-T_{Bt}\right)=0\ , \tag{26}$$

$$\hat{z}=-h/2:\ -k(\hat{x},\hat{y},\hat{z}=-h/2)\left.\frac{dT(\hat{x},\hat{y},\hat{z})}{d\hat{z}}\right|_{\hat{z}=-h/2}-h_{ct}\left(T(\hat{x},\hat{y},\hat{z}=-h/2)-T_{Bb}\right)=0\ . \tag{27}$$

In (25) K^* is given by

$$K^*=Kk(\hat{z}), \tag{28}$$

where K represents an unknown constant. The inclusion of (28) in (25) is mandatory for accurate results and is in contrast to [11] where a similar strong form is used without K^*. The inclusion of K^* can be motivated by the following thought experiment: Within a shell's section of constant conductivity the transverse temperature distribution is expected to be parabolic with prescribed gradients at the top and bottom surface. In absence of K^* the solution of (25) leads to a linear distribution and (26) and (27) cannot be satisfied exactly. The introduction of a non-vanishing constant K^* avoids such a deficiency. The unknown constant K is found from the

[1] Within one element the thermal conduction coefficient k is assumed to be constant, however, k can be discontinuous from element to element.

constraint that the mean value of $T(\hat{x},\hat{y},\hat{z})$ must equal $\bar{T}(\hat{x},\hat{y})$ from (12). Rewriting (25)-(27) with $T(\hat{x},\hat{y},\hat{z}) = \bar{T}(\hat{x},\hat{y}) + \widetilde{T}(\hat{z})$ leads to

$$\frac{d}{d\hat{z}}\left(k(\hat{x},\hat{y},\hat{z})\frac{d}{d\hat{z}}\widetilde{T}(\hat{z})\right) + Kk(\hat{z}) = 0 \ , \tag{29}$$

$$\hat{z} = {}^{h}/_{2}: \ -k(\hat{x},\hat{y},\hat{z}={}^{h}/_{2})\left.\frac{d\widetilde{T}(\hat{z})}{d\hat{z}}\right|_{\hat{z}={}^{h}/_{2}} - h_{ct}\left(\bar{T}(\hat{x},\hat{y}) + \widetilde{T}(\hat{z}=-{}^{h}/_{2}) - T_{Bt}\right) = 0 \ , \tag{30}$$

$$\hat{z} = -{}^{h}/_{2}: \ -k(\hat{x},\hat{y},\hat{z}=-{}^{h}/_{2})\left.\frac{d\widetilde{T}(\hat{z})}{d\hat{z}}\right|_{\hat{z}=-{}^{h}/_{2}} - h_{ct}\left(\bar{T}(\hat{x},\hat{y}) + \widetilde{T}(\hat{z}=-{}^{h}/_{2}) - T_{Bb}\right) = 0 \ , \tag{31}$$

$$\int_{h} \widetilde{T}(\hat{z})\, d\hat{z} = 0 \ . \tag{32}$$

An analytical solution of (29)-(32) can be given in case of a constant conductivity, i.e. $k(\hat{z}) = k$, however, for arbitrary variations of $k(\hat{z})$ we propose a FEM like solution procedure using a discretization with n linear elements of length $l_e = {}^{h}/_{n}$, see Fig. 3(b). Hence, we find for interior elements

$$dA\int_{l_e} k(\hat{z})\widetilde{T}_{,\hat{z}}\delta\widetilde{T}_{,\hat{z}}\, d\hat{z} = dAK\int_{l_e} k(\hat{z})\delta\widetilde{T}\, d\hat{z}, \tag{33}$$

and for the top and bottom elements

$$\text{bottom}\ (\hat{z}=-{}^{h}/_{2}): \ dA\int_{l_e} k(\hat{z})\widetilde{T}_{,\hat{z}}\delta\widetilde{T}_{,\hat{z}}\, d\hat{z} = dA\int_{l_e} K^{*}\delta\widetilde{T}\, d\hat{z} - \left(h_{cb}dA\left(\bar{T}+\widetilde{T}-T_{Bb}\right)\delta\widetilde{T}\right)\Big|_{\hat{z}=-{}^{h}/_{2}}, \tag{34}$$

$$\text{top}\ (\hat{z}={}^{h}/_{2}): \ dA\int_{l_e} k(\hat{z})\widetilde{T}_{,\hat{z}}\delta\widetilde{T}_{,\hat{z}}\, d\hat{z} = dA\int_{l_e} K^{*}\delta\widetilde{T}\, d\hat{z} - \left(h_{ct}dA\left(\bar{T}+\widetilde{T}-T_{Bt}\right)\delta\widetilde{T}\right)\Big|_{\hat{z}={}^{h}/_{2}}, \tag{35}$$

where $k(\hat{z})$ is assumed to the be the value of thermal conductivity at each element's center, being constant throughout each element. This finally leads to the following system of equations

$$\left\{\frac{n}{h}\begin{bmatrix} k_1 & \cdots & 0 & 0 \\ \vdots & \ddots & \vdots & \vdots \\ 0 & \cdots & k_{n-1} & -k_n \\ 0 & \cdots & -k_n & k_n \end{bmatrix} + \begin{bmatrix} h_{cb} & \cdots & 0 & 0 \\ \vdots & \ddots & \vdots & \vdots \\ 0 & \cdots & 0 & 0 \\ 0 & \cdots & 0 & h_{ct} \end{bmatrix}\right\}\begin{bmatrix} \vartheta_1 \\ \vdots \\ \vartheta_n \\ \vartheta_{n+1} \end{bmatrix} =$$

$$= \frac{K\,h}{2n}\begin{bmatrix} k_1 \\ \vdots \\ k_{n-1} \\ k_n \end{bmatrix} + \begin{bmatrix} h_{cb}\left(T_{Bb}-\bar{T}\right) \\ \vdots \\ 0 \\ h_{ct}\left(T_{Bt}-\bar{T}\right) \end{bmatrix}, \tag{36}$$

where ϑ_i for $i = 1...n+1$ denotes the nodal value of $\widetilde{T}$ and k_i for $i = 1...n$ refers to the thermal conductivity at the i-th element's center. Equation (36) can be rewritten according to

$$\mathbf{K}\boldsymbol{\vartheta} = K\mathbf{F} + \mathbf{F}_c, \tag{37}$$

and represents a linear algebraic system of equations approximating (29)-(31). Equation (32) is modeled as

$$\frac{1}{2}\left(\vartheta_1 + \vartheta_{n+1}\right) + \sum_{i=2}^{n} \vartheta_i = \left[\begin{array}{cccc} 1/2 & \cdots & 1 & 1/2 \end{array}\right] \left[\begin{array}{c} \vartheta_1 \\ \vdots \\ \vartheta_n \\ \vartheta_{n+1} \end{array}\right] = \mathbf{L}\boldsymbol{\vartheta} = 0, \tag{38}$$

and can be used to evaluate the unknown constant K,

$$K = -\frac{\mathbf{L}\mathbf{K}^{-1}\mathbf{F}_c}{\mathbf{L}\mathbf{K}^{-1}\mathbf{F}}, \tag{39}$$

consequently, the nodal values $\boldsymbol{\vartheta}$ read

$$\boldsymbol{\vartheta} = -\frac{\mathbf{L}\mathbf{K}^{-1}\mathbf{F}_c}{\mathbf{L}\mathbf{K}^{-1}\mathbf{F}}\mathbf{K}^{-1}\mathbf{F} + \mathbf{K}^{-1}\mathbf{F}_c. \tag{40}$$

2.2 Mechanical analysis

The derivation of a six parameter shell element is based on four steps. In Sect. 2.2.1 we present useful equations for evaluating effective elastic quantities. Arbitrary warped element geometries show a computationally expensive coupling between membrane and bending properties. In order to avoid the derivation of those coupling matrices, we describe in Sect. 2.2.2 a projection scheme, which extracts a plane element configuration. Using that projection the derivation of the stiffness matrix can be separated into a membrane (Sect. 2.2.3) and a bending part (Sect. 2.2.4).

2.2.1 Effective elastic quantities

The element formulation requires four effective quantities that are directly related to the distribution of Young's modulus $E(\hat{z})$. We present here only the main results and refer to [15] for details. In case of unsymmetrical variations of E the offset $\overline{z}$ of a neutral surface from the discretized mid-plane is evaluated as

$$\overline{z} = \frac{\int_{-h/2}^{h/2} E(\hat{z})\hat{z}d\hat{z}}{\int_{-h/2}^{h/2} E(\hat{z})d\hat{z}}. \tag{41}$$

With respect to this plane, membrane and bending deformations are decoupled and an arbitrary normal strain reads

$$\varepsilon_{ij}(\hat{z}') = \varkappa_{ij}\hat{z}' + \varepsilon_{ij}^{(0)}, \tag{42}$$

with $\hat{z}' = \hat{z} - \overline{z}$. In (42) $\varepsilon_{ij}^{(0)}$ denotes the strain in the neutral surface and $\varkappa_{ij}$ refers to a curvature. The effective moduli for membrane (E_m) and bending (E_b) read

$$E_m = \frac{1}{h}\int_{-h/2-\overline{z}}^{h/2-\overline{z}} E(\hat{z}')d\hat{z}', \tag{43}$$

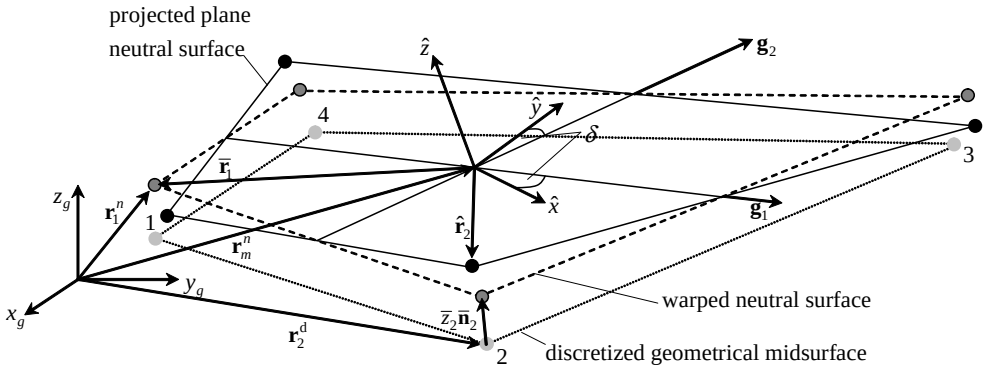

Figure 4: Discretized mid-surface, warped neutral surface, projected plane neutral surface

$$E_b = \frac{12}{h^3} \int\limits_{-h/2-\overline{z}}^{h/2-\overline{z}} E(\hat{z}')\hat{z}'^2 d\hat{z}'. \tag{44}$$

Since shear deformations are accounted for, a shear correction factor α_s is to be introduced. For homogenous shells $\alpha_s = 5/6$, while in case of varying $E(\hat{z})$ one finds [15]

$$\frac{1}{\alpha_s} = \frac{144}{E_b h^5} \int\limits_{-h/2-\overline{z}}^{h/2-\overline{z}} \frac{1}{E(\hat{z}')} \left[\int\limits_{\hat{z}'}^{h/2-\overline{z}} E(\zeta)\zeta d\zeta \right]^2 d\hat{z}'. \tag{45}$$

2.2.2 A projection scheme

We decouple the membrane and bending properties in two steps. Firstly, we shift the element configuration, which is discretizing the geometrical mid-plane to the mechanical neutral surface (41). According to Fig. 4 this is done via

$$\mathbf{r}_i^n = \mathbf{r}_i^d + \overline{z}_i \overline{\mathbf{n}}_i \quad \text{no sum on } i, \tag{46}$$

where $\mathbf{r}_i^d$ and $\mathbf{r}_i^n$ denote the coordinates of the i-th node ($i = 1, 2, 3, 4$) of the discretized and the neutral surface. The projection is carried out along a nodal fiber direction $\overline{\mathbf{n}}_i$, which can be extracted from the preprocessor or can be found with the aid of an algorithm discussed in [15]. Since the element configuration discretizing the neutral surface may be warped, we extract a plane element configuration as shown in Fig. 4. A local Cartesian coordinate system $\hat{x} - \hat{y} - \hat{z}$ is placed at the element's center point with $\mathbf{r}_m^n = \frac{1}{4}\sum_{i=1}^4 \mathbf{r}_i^n$. The base vectors $\mathbf{e}_{\hat{x}}$ and $\mathbf{e}_{\hat{y}}$ share an equal angle δ to $\mathbf{g}_1$ and $\mathbf{g}_2$, which join the center and the mid-side points (Fig. 4). Finally, the nodes are projected onto the $\hat{\mathbf{e}}_x - \hat{\mathbf{e}}_y$ plane giving a plane element with local nodal vectors $\hat{\mathbf{r}}_i = \begin{bmatrix} \hat{X}_i & \hat{Y}_i & 0 \end{bmatrix}^T$ as depicted in Fig. 1. The proposed projection scheme may introduce some rigid body error. This problem is indicated by many authors, e.g. [21, 22] and can easily be corrected by a method proposed by Rankin and Nour-Omid [23]. The details of this procedure are discussed in [12, 24], we only give the final result

$$\hat{\mathbf{K}}_{proj} = \hat{\mathbf{P}}_R^T \hat{\mathbf{K}} \hat{\mathbf{P}}_R, \tag{47}$$

with $\hat{\mathbf{P}}_R = \left[\mathbf{I}_{(24\times24)} - \hat{\mathfrak{R}}\left(\hat{\mathfrak{R}}^T\hat{\mathfrak{R}}\right)^{-1}\hat{\mathfrak{R}}^T\right]$ denoting the projection with

$$\hat{\mathfrak{R}} = \begin{bmatrix} \hat{\mathfrak{R}}_1 \\ \hat{\mathfrak{R}}_2 \\ \hat{\mathfrak{R}}_3 \\ \hat{\mathfrak{R}}_4 \end{bmatrix} \quad \text{with} \quad \hat{\mathfrak{R}}_i = \begin{bmatrix} 1 & 0 & 0 & 0 & \hat{Z}_i & -\hat{Y}_i \\ 0 & 1 & 0 & -\hat{Z}_i & 0 & \bar{X}_i \\ 0 & 0 & 1 & \hat{Y}_i & -\bar{X}_i & 0 \\ 0 & 0 & 0 & 1 & 0 & 0 \\ 0 & 0 & 0 & 0 & 1 & 0 \\ 0 & 0 & 0 & 0 & 0 & 1 \end{bmatrix}. \tag{48}$$

The parts of the element stiffness matrix

$$\hat{\mathbf{K}} = \begin{bmatrix} \hat{\mathbf{K}}_{membrane} & \mathbf{0} \\ \mathbf{0} & \hat{\mathbf{K}}_{plate} \end{bmatrix} \tag{49}$$

are derived in Sect. 2.2.3 and Sect. 2.2.4, while the global stiffness matrix $\widetilde{\mathbf{K}}$ is assembled after a transformation of $\hat{\mathbf{K}}_{proj}$ to the global Cartesian coordinate system. Note that $\widetilde{\mathbf{K}}$ refers to the mechanical neutral surface (41), while the load vector is usually applied onto the discretized mid-plane. Therefore, an element load vector applied onto the mid-surface $\left[\begin{array}{cc} \mathbf{F}^d & \mathbf{M}^d \end{array}\right]^T$ has to be reduced to a force vector, which refers the neutral surface $\left[\begin{array}{cc} \mathbf{F}^n & \mathbf{M}^n \end{array}\right]^T$ via

$$\mathbf{F}^n = \mathbf{F}^d \quad \text{and} \quad \mathbf{M}^n = \mathbf{M}^d - \overline{z}_i\overline{\mathbf{n}}_i \times \mathbf{F}^d. \tag{50}$$

After solving the global system of equations the resulting displacements $\mathbf{U}^n$ and rotations $\boldsymbol{\phi}^n$ also refer to the neutral surface. During post-processing at the discretized configuration, a transformation according to

$$\mathbf{U}^d = \mathbf{U}^n + \overline{z}_i\overline{\mathbf{n}}_i \times \boldsymbol{\phi}^n \quad \text{and} \quad \boldsymbol{\phi}^d = \boldsymbol{\phi}^n \tag{51}$$

has to be carried out [15].

2.2.3 The membrane part

The inclusion of drill rotations, i.e. the rotation about the shell's normal, is a main issue of this paper. These in-plane rotational degrees of freedom are introduced using a recently proposed Cosserat-type functional [13, 12],

$$\delta\Pi_{membrane} = h\int_{\Omega} \delta\hat{\overline{\boldsymbol{\varepsilon}}}_s^T\hat{\mathbf{C}}_m\hat{\overline{\boldsymbol{\varepsilon}}}_s dA_e + 2\alpha h\int_{\Omega} \delta\hat{\overline{\varepsilon}}_a\hat{\overline{\varepsilon}}_a dA_e. \tag{52}$$

In (52), $\hat{\overline{\boldsymbol{\varepsilon}}}_s$ and $\hat{\overline{\varepsilon}}_a$ denote the symmetric and the antimetric part of the membrane strain tensor, respectively. The overbar indicates assumed strains, which can be assumed independently and are not directly related to prescribed deformations and rotations,

$$\hat{\boldsymbol{\varepsilon}}_s = \left[\begin{array}{ccc} u_{\hat{x},\hat{x}} & u_{\hat{y},\hat{y}} & u_{\hat{x},\hat{y}} + u_{\hat{y},\hat{x}} \end{array}\right]^T \quad \text{and} \quad \hat{\varepsilon}_a = {}^1\!/_2\left(u_{\hat{x},\hat{y}} - u_{\hat{y},\hat{x}}\right) + \varphi_{\hat{z}}. \tag{53}$$

For sake of convenience the direct strain-displacement-relation is given in (53), where u_i for $i = \hat{x}, \hat{y}$ and $\varphi_{\hat{z}}$ refer to membrane displacements and drill rotations, respectively. In (52) A_e denotes the area of the element (8) and $\hat{\mathbf{C}}_m$ refers to the plane stress elasticity matrix (43)

$$\hat{\mathbf{C}}_m = \frac{E_m}{1-\nu^2}\begin{bmatrix} 1 & \nu & 0 \\ \nu & 1 & 0 \\ 0 & 0 & \frac{1-\nu}{2} \end{bmatrix}. \tag{54}$$

The variable α represents an additional material constant relating the skew symmetric parts of stresses and strains. As frequently recommended (e.g. [14]), this constitutive parameter can be related to the shear modulus of the corresponding material,

$$\alpha = \overline{\alpha}\frac{E_m}{2\left(1+\nu\right)}, \tag{55}$$

where $\overline{\alpha}$ denotes an additional scaling factor. The present formulation can be optimized according to accuracy and efficiency, while avoiding any internal (incompatible) degrees of freedom to circumvent membrane shear locking in low order elements [18]. The predictive quality is nearly independent of $\overline{\alpha}$ and suitable scaling factors are discussed in [12]. The assumed strain fields are related to nodal displacements and rotations, i.e.

$$\hat{\overline{\boldsymbol{\varepsilon}}}_s = \hat{\overline{\mathbf{B}}}_{su0}\begin{bmatrix}\mathbf{U}_{\hat{x}}\\ \mathbf{U}_{\hat{y}}\end{bmatrix} + \hat{\overline{\mathbf{B}}}_{suH}\begin{bmatrix}\boldsymbol{\gamma} & \mathbf{0}\\ \mathbf{0} & \boldsymbol{\gamma}\end{bmatrix}\begin{bmatrix}\mathbf{U}_{\hat{x}}\\ \mathbf{U}_{\hat{y}}\end{bmatrix}, \tag{56}$$

$$\hat{\overline{\varepsilon}}_a = \frac{1}{2}\left(\hat{\overline{\mathbf{B}}}_{au0}\begin{bmatrix}\mathbf{U}_{\hat{x}}\\ \mathbf{U}_{\hat{y}}\end{bmatrix} + \hat{\overline{\mathbf{B}}}_{auH}\begin{bmatrix}\boldsymbol{\gamma} & \mathbf{0}\\ \mathbf{0} & \boldsymbol{\gamma}\end{bmatrix}\begin{bmatrix}\mathbf{U}_{\hat{x}}\\ \mathbf{U}_{\hat{y}}\end{bmatrix}\right) + \overline{\mathbf{N}}_{\varphi}\hat{\boldsymbol{\Phi}}, \tag{57}$$

where $\mathbf{U}_{\hat{x}} = \begin{bmatrix}\mathbf{U}_{\hat{x}1} & \cdots & \mathbf{U}_{\hat{x}4}\end{bmatrix}^T$ and $\mathbf{U}_{\hat{y}} = \begin{bmatrix}\mathbf{U}_{\hat{y}1} & \cdots & \mathbf{U}_{\hat{y}4}\end{bmatrix}^T$ are the inplane nodal displacements while $\hat{\boldsymbol{\Phi}} = \begin{bmatrix}\phi_{\hat{z}1} & \cdots & \phi_{\hat{z}4}\end{bmatrix}$ contains the drill rotation angles. The corresponding $\hat{\overline{\mathbf{B}}}$-matrices and the shape functions $\overline{\mathbf{N}}_{\varphi}$ read

$$\hat{\overline{\mathbf{B}}}_{su0} = \sqrt{\frac{j_0}{j}}\begin{bmatrix}\mathbf{b}_x & \mathbf{0}\\ \mathbf{0} & \mathbf{b}_y\\ \mathbf{b}_y & \mathbf{b}_x\end{bmatrix}, \quad \hat{\overline{\mathbf{B}}}_{suH} = \sqrt{\frac{j}{j_0}}\begin{bmatrix}\left(\xi\eta\right)_{,\hat{x}} & -\nu\left(\xi\eta\right)_{,\hat{y}}\\ -\nu\left(\xi\eta\right)_{,\hat{x}} & \left(\xi\eta\right)_{,\hat{y}}\\ 0 & 0\end{bmatrix}, \tag{58}$$

$$\hat{\overline{\mathbf{B}}}_{au0} = \sqrt{\frac{j_0}{j}}\begin{bmatrix}\mathbf{b}_y & -\mathbf{b}_x\end{bmatrix}, \quad \hat{\overline{\mathbf{B}}}_{auH} = 2\sqrt{\frac{j}{j_0}}\begin{bmatrix}\left(\xi\eta\right)_{,\hat{y}} & -\left(\xi\eta\right)_{,\hat{x}}\end{bmatrix}, \tag{59}$$

$$\overline{\mathbf{N}}_{\varphi} = \sqrt{\frac{j_0}{j}}\begin{bmatrix}N_1 & N_2 & N_3 & N_4\end{bmatrix}, \tag{60}$$

where $j = \det\mathbf{J}$ and $j_0 = \det\mathbf{J}_0 = \det\mathbf{J}(\xi=\eta=0)$ (see (2) - (8)). The prefactors $\sqrt{j/j_0}$ and $\sqrt{j_0/j}$ enable an analytical integration of all parts of the membrane stiffness matrix avoiding a four point Gaussian quadrature. The resulting membrane part of the stiffness matrix may be found in [25].

2.2.4 The bending part

The bending part of the stiffness matrix is based on the Mindlin-Reissner hypothesis and is valid for thin to moderately thick shell structures [17, 24, 12]. Equilibrium requires the potential Π_{plate} to be a minimum, i.e.

$$\Pi_{plate} = \Pi_b + \Pi_s - \Pi_{ext} \;\rightarrow \min, \tag{61}$$

with

$$\Pi_b = \frac{1}{2}\int\limits_{\Omega}\hat{\overline{\boldsymbol{\epsilon}}}_b^T\hat{\mathbf{C}}_b\hat{\overline{\boldsymbol{\epsilon}}}_b d\Omega,$$

$$\Pi_s = \frac{1}{2}\alpha_s h \frac{E_b}{2(1+\nu)} \int\limits_{A_e} \hat{\overline{\boldsymbol{\gamma}}}_s^T \hat{\overline{\boldsymbol{\gamma}}}_s dA,$$

$$\Pi_{ext} = \int\limits_{A_e} p u_{\hat{z}} dA. \tag{62}$$

An overbar again indicates that the corresponding field can be interpolated independently, i.e. without any relation to strain displacement equations. The subscripts b and s indicate that the corresponding quantity refers to bending and shear, respectively, and Π_{ext} is due to the externally applied pressures p. The variables $\hat{\overline{\boldsymbol{\epsilon}}}_b$ and $\hat{\overline{\boldsymbol{\gamma}}}_s$ denote bending and transverse shear strains. In (62) $\hat{\mathbf{C}}_b$ refers to the bilinear plane stress elasticity matrix (44)

$$\hat{\mathbf{C}}_b = \frac{E_b}{1-\nu^2} \begin{bmatrix} 1 & \nu & 0 \\ \nu & 1 & 0 \\ 0 & 0 & \frac{1-\nu}{2} \end{bmatrix}, \tag{63}$$

while α_s denotes the shear correction factor (45). Following the procedure in [12, 24], the corresponding interpolations read

$$\hat{\overline{\boldsymbol{\epsilon}}}_b = \hat{\overline{\mathbf{B}}}_{b0} \begin{bmatrix} \boldsymbol{\Phi}_{\hat{x}} \\ \boldsymbol{\Phi}_{\hat{y}} \end{bmatrix} + \hat{\overline{\mathbf{B}}}_{bH} \begin{bmatrix} \boldsymbol{\gamma} & \mathbf{0} \\ 0 & \boldsymbol{\gamma} \end{bmatrix} \begin{bmatrix} \boldsymbol{\Phi}_{\hat{x}} \\ \boldsymbol{\Phi}_{\hat{y}} \end{bmatrix}, \tag{64}$$

with

$$\hat{\overline{\mathbf{B}}}_{b0} = \hat{z}\sqrt{\frac{j_0}{j}} \begin{bmatrix} \mathbf{0} & \mathbf{b}_x^T \\ -\mathbf{b}_y^T & \mathbf{0} \\ -\mathbf{b}_x^T & \mathbf{b}_y^T \end{bmatrix}, \quad \hat{\overline{\mathbf{B}}}_{bH} = \hat{z}\sqrt{\frac{j}{j_0}} \begin{bmatrix} \nu\,(\xi\eta)_{,\hat{y}} & (\xi\eta)_{,\hat{x}} \\ -\,(\xi\eta)_{,\hat{y}} & -\nu\,(\xi\eta)_{,\hat{x}} \\ 0 & 0 \end{bmatrix}, \tag{65}$$

and

$$\hat{\overline{\boldsymbol{\gamma}}}_s = \mathbf{J}_0^{-1} \mathbf{N}_s \boldsymbol{\Gamma} \tag{66}$$

with

$$\mathbf{N}_s = \sqrt{\frac{j_0}{j}} \begin{bmatrix} \frac{1}{2}(1-\eta) & 0 & \frac{1}{2}(1+\eta) & 0 \\ 0 & \frac{1}{2}(1+\xi) & 0 & \frac{1}{2}(1-\xi) \end{bmatrix}$$

and $\boldsymbol{\Gamma} = \mathbf{A}_{uz}\mathbf{U}_{\hat{z}} + \mathbf{A}_{\varphi x}\boldsymbol{\Phi}_{\hat{x}} + \mathbf{A}_{\varphi y}\boldsymbol{\Phi}_{\hat{y}}$. The coefficients $\mathbf{A}_{uz}$, $\mathbf{A}_{\varphi x}$ and $\mathbf{A}_{\varphi y}$ only depend on the element's geometry and read

$$\mathbf{A}_{uz} = \frac{1}{2} \begin{bmatrix} -1 & 1 & 0 & 0 \\ -1 & 0 & 0 & 1 \\ 0 & 0 & 1 & -1 \\ 0 & -1 & 1 & 0 \end{bmatrix},$$

$$\mathbf{A}_{\varphi x} = \frac{1}{4} \begin{bmatrix} \hat{y}_{12} & \hat{y}_{12} & 0 & 0 \\ \hat{y}_{14} & 0 & 0 & \hat{y}_{14} \\ 0 & 0 & \hat{y}_{43} & \hat{y}_{43} \\ 0 & \hat{y}_{23} & \hat{y}_{23} & 0 \end{bmatrix}, \; \mathbf{A}_{\varphi y} = \frac{1}{4} \begin{bmatrix} \hat{x}_{21} & \hat{x}_{21} & 0 & 0 \\ \hat{x}_{41} & 0 & 0 & \hat{x}_{41} \\ 0 & 0 & \hat{x}_{34} & \hat{x}_{34} \\ 0 & \hat{x}_{32} & \hat{x}_{32} & 0 \end{bmatrix}, \tag{67}$$

leading to a formulation, which ensures the satisfaction of the Kirchhoff patch test [26, 27]. Again, the prefactors $\sqrt{j/j_0}$ and $\sqrt{j_0/j}$ enable an analytical integration of all parts of the plate bending stiffness matrix, see e.g. [25].

2.3 Weak one-way coupling

The finite element formulation discussed in Sect. 2.2 is based on a weak form of the equilibrium conditions,

$$\delta\Pi = \int (\delta\boldsymbol{\varepsilon})^T \boldsymbol{\sigma} dV - \delta\Pi_{ext} = 0, \tag{68}$$

where any external loads are neglected in this paper[2]. The strain field in membrane directions reads

$$\begin{aligned}
\varepsilon_{\hat{x}\hat{x}} &= \frac{1}{E(\hat{z})}(\sigma_{\hat{x}\hat{x}} - \nu\sigma_{\hat{y}\hat{y}}) + \alpha(\hat{z})\Delta T(\hat{z}),\\
\varepsilon_{\hat{y}\hat{y}} &= \frac{1}{E(\hat{z})}(\sigma_{\hat{y}\hat{y}} - \nu\sigma_{\hat{x}\hat{x}}) + \alpha(\hat{z})\Delta T(\hat{z}),\\
\varepsilon_{\hat{z}\hat{z}} &= \frac{-\nu}{E(\hat{z})}(\sigma_{\hat{x}\hat{x}} + \sigma_{\hat{y}\hat{y}}) + \alpha(\hat{z})\Delta T(\hat{z}),\\
\gamma_{\hat{x}\hat{y}} &= \frac{2(1+\nu)}{E(\hat{z})}\sigma_{\hat{x}\hat{y}},
\end{aligned} \tag{69}$$

where we adopted a plane stress constraint, i.e. $\sigma_{\hat{z}\hat{z}} = 0$. The thermal expansion coefficient shows an arbitrary variation with respect to the thickness direction and is denoted by $\alpha(\hat{z})$. Solving (69) for the stresses yields

$$\begin{aligned}
\sigma_{\hat{x}\hat{x}} &= \frac{E(\hat{z})}{1-\nu^2}(\varepsilon_{\hat{x}\hat{x}} + \nu\varepsilon_{\hat{y}\hat{y}}) - \frac{E(\hat{z})\alpha(\hat{z})\Delta T(\hat{z})}{1-\nu},\\
\sigma_{\hat{y}\hat{y}} &= \frac{E(\hat{z})}{1-\nu^2}(\varepsilon_{\hat{y}\hat{y}} + \nu\varepsilon_{\hat{x}\hat{x}}) - \frac{E(\hat{z})\alpha(\hat{z})\Delta T(\hat{z})}{1-\nu},\\
\sigma_{\hat{x}\hat{y}} &= \frac{E(\hat{z})}{2(1+\nu)}\gamma_{\hat{x}\hat{y}},
\end{aligned} \tag{70}$$

or in matrix notation

$$\begin{bmatrix} \sigma_{\hat{x}\hat{x}} \\ \sigma_{\hat{y}\hat{y}} \\ \sigma_{\hat{x}\hat{y}} \end{bmatrix} = \frac{E(\hat{z})}{1-\nu^2}\begin{bmatrix} 1 & \nu & 0 \\ \nu & 1 & 0 \\ 0 & 0 & \frac{1-\nu}{2} \end{bmatrix}\begin{bmatrix} \epsilon_{\hat{x}\hat{x}} \\ \epsilon_{\hat{y}\hat{y}} \\ \epsilon_{\hat{x}\hat{y}} \end{bmatrix} - \frac{E(\hat{z})\alpha(\hat{z})\Delta T(\hat{z})}{1-\nu}\begin{bmatrix} 1 \\ 1 \\ 0 \end{bmatrix},$$

$$\boldsymbol{\sigma} = \mathbf{C}\boldsymbol{\varepsilon} - \frac{E(\hat{z})\alpha(\hat{z})\Delta T(\hat{z})}{1-\nu}\begin{bmatrix} 1 \\ 1 \\ 0 \end{bmatrix}. \tag{71}$$

Within the proposed weak one way coupling procedure we introduce (71) into (68) obtaining

$$\delta\Pi = \delta\Pi_m - \delta\Pi_t = \int\limits_{V_e} (\delta\boldsymbol{\varepsilon})^T \mathbf{C}\boldsymbol{\varepsilon} dV - \int\limits_{V_e} (\delta\boldsymbol{\varepsilon})^T \frac{E(\hat{z})\alpha(\hat{z})\Delta T(\hat{z})}{1-\nu}\begin{bmatrix} 1 \\ 1 \\ 0 \end{bmatrix} dV = 0. \tag{72}$$

[2]The inclusion of external loads can be done in a standard manner [18] and does not introduce any complications.

The first term on the RHS is devoted to the element stiffness matrix (Sect. 2.2.3 and Sect. 2.2.4), while the second part refers to internal forces and couples caused by thermal loading, which can be simplified according to

$$\delta\Pi_t = \int\limits_{V_e} \left[\begin{array}{cc} \delta\epsilon_{\hat{x}\hat{x}} & \delta\epsilon_{\hat{y}\hat{y}} \end{array}\right] \frac{E(\hat{z})\alpha(\hat{z})\Delta T(\hat{z})}{1-\nu} \left[\begin{array}{c} 1 \\ 1 \end{array}\right] dV. \tag{73}$$

The virtual normal-strain field is related to virtual displacements and rotations according to $\left[\begin{array}{cc} \delta\epsilon_{\hat{x}\hat{x}} & \delta\epsilon_{\hat{y}\hat{y}} \end{array}\right] = \left[\begin{array}{cc} \delta u_{\hat{x},\hat{x}} + \hat{z}\varphi_{\hat{y},\hat{x}} & \delta u_{\hat{y},\hat{y}} - \hat{z}\varphi_{\hat{x},\hat{y}} \end{array}\right]$. Interpolating the displacement and rotation field with classical bilinear shape-function (2),

$$\left[\begin{array}{c} u_{\hat{x}} \\ u_{\hat{y}} \end{array}\right] = \left[\begin{array}{cc} \mathbf{N} & \mathbf{0} \\ \mathbf{0} & \mathbf{N} \end{array}\right] \left[\begin{array}{c} \mathbf{U}_{\hat{x}} \\ \mathbf{U}_{\hat{y}} \end{array}\right] \quad \text{and} \quad \left[\begin{array}{c} \varphi_{\hat{x}} \\ \varphi_{\hat{y}} \end{array}\right] = \left[\begin{array}{cc} \mathbf{N} & \mathbf{0} \\ \mathbf{0} & \mathbf{N} \end{array}\right] \left[\begin{array}{c} \mathbf{\Phi}_{\hat{x}} \\ \mathbf{\Phi}_{\hat{y}} \end{array}\right], \tag{74}$$

leads to

$$\delta\Pi_t = \left[\begin{array}{cc} \delta\mathbf{U}_{\hat{x}}^T & \delta\mathbf{U}_{\hat{y}}^T \end{array}\right] \left[\begin{array}{c} \mathbf{F}_{\hat{x}} \\ \mathbf{F}_{\hat{y}} \end{array}\right] + \left[\begin{array}{cc} \delta\mathbf{\Phi}_{\hat{x}}^T & \delta\mathbf{\Phi}_{\hat{y}}^T \end{array}\right] \left[\begin{array}{c} \mathbf{M}_{\hat{x}} \\ \mathbf{M}_{\hat{y}} \end{array}\right], \tag{75}$$

with

$$\begin{aligned} \mathbf{F}_{\hat{x}} &= \int\limits_{V_e} \mathbf{N}_{,\hat{x}} \frac{E(\hat{z})\alpha(\hat{z})\Delta T(\hat{z})}{1-\nu} dV \quad , \quad \mathbf{F}_{\hat{y}} = \int\limits_{V_e} \mathbf{N}_{,\hat{y}} \frac{E(\hat{z})\alpha(\hat{z})\Delta T(\hat{z})}{1-\nu} dV, \\ \mathbf{M}_{\hat{x}} &= -\int\limits_{V_e} \mathbf{N}_{,\hat{y}} \hat{z} \frac{E(\hat{z})\alpha(\hat{z})\Delta T(\hat{z})}{1-\nu} dV \quad , \quad \mathbf{M}_{\hat{y}} = \int\limits_{V_e} \mathbf{N}_{,\hat{x}} \hat{z} \frac{E(\hat{z})\alpha(\hat{z})\Delta T(\hat{z})}{1-\nu} dV. \end{aligned} \tag{76}$$

Differentiating the shape functions indicates that the integral over the element area can be carried out analytically, if the distributions of Young's modulus E, thermal expansion α and temperature ΔT are assumed to be constant. Thus, we get

$$\begin{aligned} \mathbf{F}_{\hat{x}} &= \frac{1}{2} \left[\begin{array}{c} \hat{y}_{24} \\ \hat{y}_{31} \\ \hat{y}_{42} \\ \hat{y}_{13} \end{array}\right] \int\limits_{-h/2}^{h/2} \frac{E(\hat{z})\alpha(\hat{z})\Delta T(\hat{z})}{1-\nu} d\hat{z} \quad , \quad \mathbf{F}_{\hat{y}} = \frac{1}{2} \left[\begin{array}{c} \hat{x}_{42} \\ \hat{x}_{13} \\ \hat{x}_{24} \\ \hat{x}_{31} \end{array}\right] \int\limits_{-h/2}^{h/2} \frac{E(\hat{z})\alpha(\hat{z})\Delta T(\hat{z})}{1-\nu} d\hat{z}, \\ \mathbf{M}_{\hat{x}} &= \frac{1}{2} \left[\begin{array}{c} \hat{x}_{24} \\ \hat{x}_{31} \\ \hat{x}_{42} \\ \hat{x}_{13} \end{array}\right] \int\limits_{-h/2}^{h/2} \hat{z} \frac{E(\hat{z})\alpha(\hat{z})\Delta T(\hat{z})}{1-\nu} d\hat{z} \quad , \quad \mathbf{M}_{\hat{y}} = \frac{1}{2} \left[\begin{array}{c} \hat{y}_{24} \\ \hat{y}_{31} \\ \hat{y}_{42} \\ \hat{y}_{13} \end{array}\right] \int\limits_{-h/2}^{h/2} \hat{z} \frac{E(\hat{z})\alpha(\hat{z})\Delta T(\hat{z})}{1-\nu} d\hat{z}. \end{aligned} \tag{77}$$

These element forces and couples refer to the discretized mid-surface and have to be transformed to the neutral surface by (50).

2.4 Stress evaluation

The stress components are evalutated element-wise at $\xi = \eta = 0$ based on an a posteriori procedure, requiring the nodal displacement and rotation vector in the elemental Cartesian base. The membrane strains at the elements center are evaluated with respect to the nodal degrees of freedom by

$$\left[\begin{array}{c} \epsilon_{\hat{x}\hat{x}} \\ \epsilon_{\hat{y}\hat{y}} \\ \gamma_{\hat{x}\hat{y}} \end{array}\right] = \left[\begin{array}{cc} \mathbf{b}_x & \mathbf{0} \\ \mathbf{0} & \mathbf{b}_y \\ \mathbf{b}_y & \mathbf{b}_x \end{array}\right] \left[\begin{array}{c} \mathbf{U}_{\hat{x}} \\ \mathbf{U}_{\hat{y}} \end{array}\right] + \hat{z}' \left[\begin{array}{cc} \mathbf{0} & \mathbf{b}_x^T \\ -\mathbf{b}_y^T & \mathbf{0} \\ -\mathbf{b}_x^T & \mathbf{b}_y^T \end{array}\right] \left[\begin{array}{c} \mathbf{\Phi}_{\hat{x}} \\ \mathbf{\Phi}_{\hat{y}} \end{array}\right]. \tag{78}$$

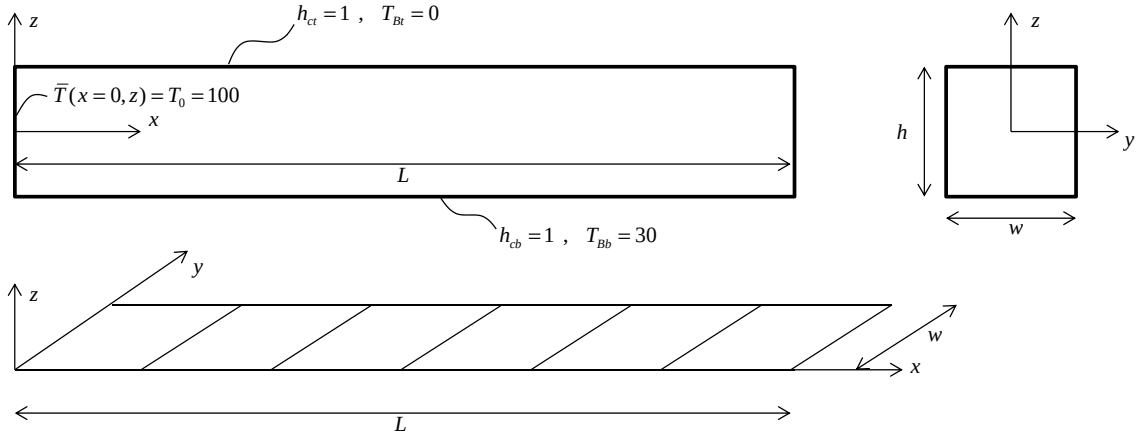

Figure 5: FGM fin with a discretization of $N = 6$

Consequently, the membrane stresses are found by applying the constitutive relation (71),

$$\begin{bmatrix} \sigma_{\hat{x}\hat{x}} \\ \sigma_{\hat{y}\hat{y}} \\ \sigma_{\hat{x}\hat{y}} \end{bmatrix} = \frac{E(\hat{z}')}{1-\nu^2} \begin{bmatrix} 1 & \nu & 0 \\ \nu & 1 & 0 \\ 0 & 0 & \frac{1-\nu}{2} \end{bmatrix} \begin{bmatrix} \epsilon_{\hat{x}\hat{x}} \\ \epsilon_{\hat{y}\hat{y}} \\ \epsilon_{\hat{x}\hat{y}} \end{bmatrix} - \frac{E(\hat{z}')\alpha(\hat{z}')\Delta T(\hat{z}')}{1-\nu} \begin{bmatrix} 1 \\ 1 \\ 0 \end{bmatrix}.$$

The definition of transverse shear strains read $\gamma_{\hat{x}\hat{z}} = u_{\hat{z},\hat{x}} + \varphi_{\hat{y}}$ and $\gamma_{\hat{y}\hat{z}} = u_{\hat{z},\hat{y}} - \varphi_{\hat{x}}$. The transverse displacement and the two bending angles are interpolated with classical bilinear shape functions yielding to the following estimates of the averaged shear strains

$$\begin{bmatrix} \overline{\gamma}_{\hat{x}\hat{z}} \\ \overline{\gamma}_{\hat{y}\hat{z}} \end{bmatrix} = \begin{bmatrix} \mathbf{b}_x \\ \mathbf{b}_y \end{bmatrix} \mathbf{U}_{\hat{z}} + \begin{bmatrix} 1/4 \sum_{i=1}^{4} \phi_{\hat{y}i} \\ -1/4 \sum_{i=1}^{4} \phi_{\hat{x}i} \end{bmatrix}. \tag{79}$$

Accordingly, the averaged shear stresses read $\overline{\tau}_{i\hat{z}} = \frac{E_b(\xi=\eta=0)}{2(1+\nu)}\overline{\gamma}_{i\hat{z}}$ for $i = \hat{x}, \hat{y}$, and the integrated shear force is given by $s_i = \alpha_s h \overline{\tau}_{i\hat{z}}$. Finally, we evaluate the shear stress distribution from

$$\tau_{i\hat{z}}(\hat{z}') = \frac{12 s_i}{E_b h^3} \int_{\hat{z}'}^{h/2-\overline{z}} E(\zeta)\zeta d\zeta \quad , \quad \gamma_{i\hat{z}}(\hat{z}') = \frac{2(1+\nu)\tau_{i\hat{z}}(\hat{z}')}{E(z')}, \tag{80}$$

see [15]

3 Benchmark examples

In this Section we compare the proposed formulation to continuum solutions evaluated by ANSYS. A main issue of this paper is the correct estimation of temperature distributions based on the procedures discussed in Sect. 2.1. Consequently, a pure thermal problem is discussed in Sect. 3.1, which shows interesting results for two MLC structures with the same mean value of thermal conductivity. More examples can be found in [25].

3.1 Temperature distributions in a MLC fin

Consider a rectangular MLC structure of length $L = 10$, width $w = 1$ and height $h = 1$ shown in Fig. 5, which is discretized with N elements. On the top and bottom surface ($z = \pm h/2$) there is convection with $h_{ct} = h_{cb} = 1$ and a fluid temperature $T_{Bt} = 0$ and $T_{Bb} = 30$, while at the left end $x = 0$ the temperature is set to $\bar{T}(x = 0, z) = T_0 = 100$.

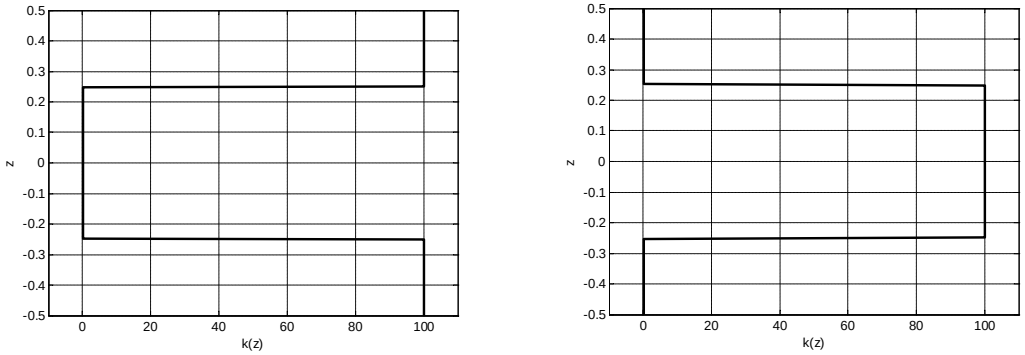

(a) Configuration 1 (b) Configuration 2

Figure 6: Distribution of thermal conductivity of layered fin

Interval in transverse direction	Configuration 1	Configuration 2
$-0.5 \leq z \leq -0.25$	$k = 100$	$k = 0.1$
$-0.25 \leq z \leq 0$	$k = 0.1$	$k = 100$
$0 \leq z \leq 0.25$	$k = 0.1$	$k = 100$
$0.25 \leq z \leq 0.5$	$k = 100$	$k = 0.1$

Table 1: Conductivity distribution

The fin is composed of four equidistant layers of height $h_L = {}^{h}/_{4}$, with two different thermal conductivities. We compare two symmetric configurations (i.e. Configuration 1 and Configuration 2) according to Tab. 1 (see Fig. 6). Configuration 1 is characterized by a high thermal conductivity on the top and bottom layer, while Configuration 2 has nearly isolating outside layers. The mean value $\overline{k}$ of thermal conductivity is equal for both configurations and classical approaches from literature assuming a constant temperature in thickness direction lead to equal temperature distributions in membrane direction for both configurations. The reference results are evaluated using ANSYS by discretizing the $x - z$ plane with 500×100 PLANE55 elements [28]. The application of the Dirichlet boundary condition, i.e. $T(x = 0, z) = T_0$, is in contrast to the applied convection boundary conditions at $x = 0$, $z = \pm {}^{h}/_{2}$, since the thermal gradient with respect to the thickness direction is not vanishing on the top and bottom side. Therefore, we apply a von Neumann boundary condition onto the ANSYS model based on Fourier's law, i.e.

$$q_n(x = 0,\, z) = -k(z)\bar{T}_{,x} = Ck(z), \tag{81}$$

where the constant C is found iteratively so that the evaluated mean value of the temperature distribution at $x = 0$ equals T_0. By this we obtain

$$\text{Config. 1: } q_n^{(1)}(x = 0,\, z) = -16.3613k(z), \tag{82}$$

$$\text{Config. 2: } q_n^{(2)}(x = 0,\, z) = -8.7069k(z). \tag{83}$$

The distribution of the mean value of temperature is depicted in Fig. 7, where we used $N = 20$ shell elements in membrane direction and ten elements through each layer in transverse direction ($n = 40$). The solid line corresponds to the present approach, while the dots refer to the ANSYS solution. Figure 7 indicates excellent accuracy of the proposed solution algorithm for

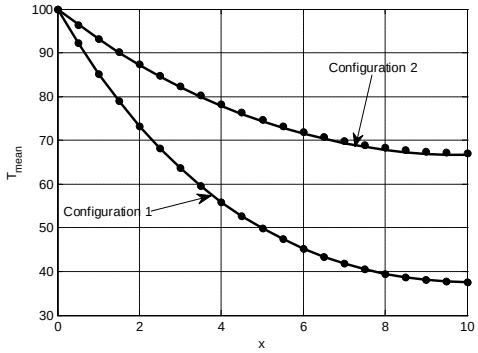

Figure 7: Mean temperature distribution of both configurations $N = 20$, $n = 40$

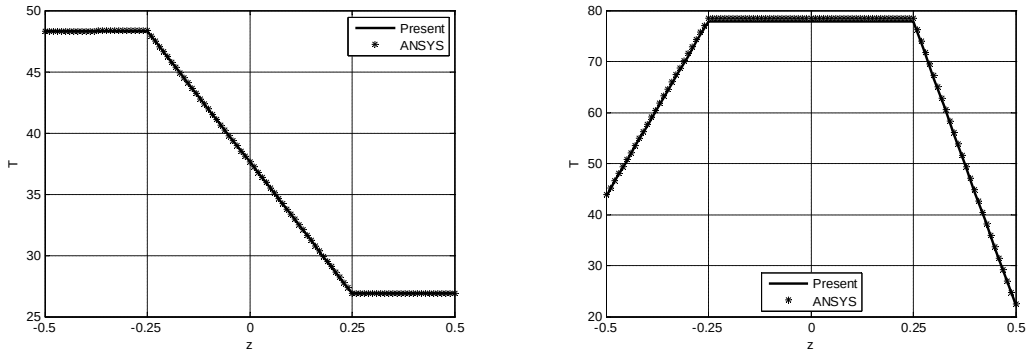

(a) Configuration 1

(b) Configuration 2

Figure 8: Temperature distribution in transverse direction at $x = L$, ($N = 20$, $n = 40$)

both configurations, and we observe large differences between the two configurations, even if the average value of the thermal conductivity is identical. The temperature distribution in transverse direction is shown in Fig. 8, and, again, indicates a good predictive quality of the proposed approach. The crucial step in our derivation is the iterative solution procedure discussed on page 5. The convergence rate is depicted in Fig. 9 for both configurations. We observe that in case of Configuration 2 (low conductivity on the top and bottom layer) about ten iterations are required to get accurate results, while Configuration 1 requires only two iterations.

3.2 Thermo-elastic analysis of a bi-quadratic FGM beam

In this example, originated by Lü et al. [29], a bi-directional FGM beam ($L = 0.1$, $h = w = 0.01$) depicted in Fig. 10 is analyzed. The state equations vary exponentially along the axial and transverse direction,

$$E(x, z) = E_0 e^{\alpha_1 x + \alpha_3 (z + h/2)}, \tag{84}$$

$$\beta(x, z) = \beta_0 e^{ax + b(z + h/2)}, \tag{85}$$

where β denotes the thermal stress constant,

$$\beta(x, z) = \frac{E(x, z)\alpha(x, z)}{1 - \nu}. \tag{86}$$

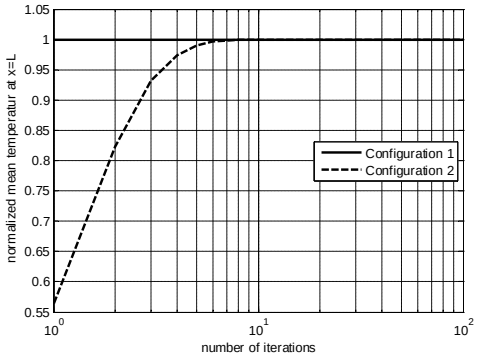

Figure 9: Convergence with respect to the number of iterations at $x = L$, ($N = 20$, $n = 40$)

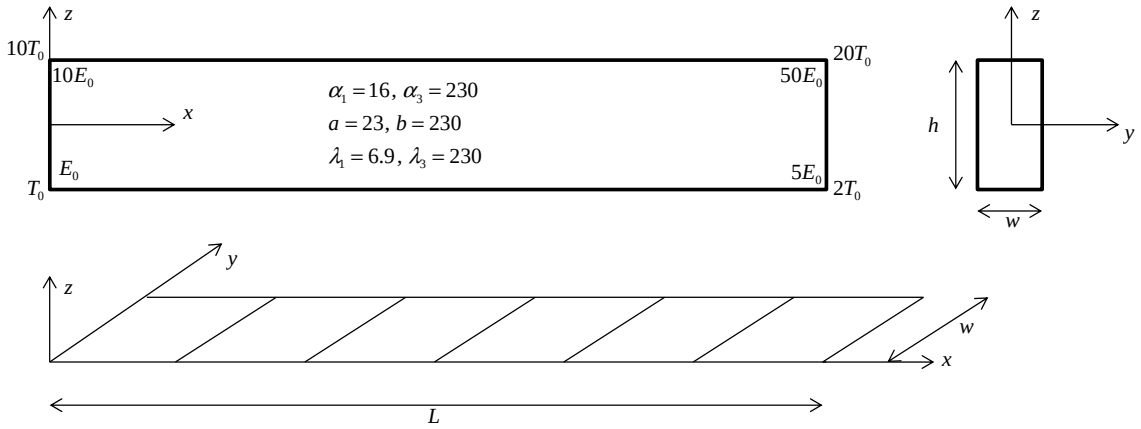

Figure 10: The schematic representation of a bi-quardratic FGM beam

Poisson's ratio is assumed to be constant $\nu = 0.25$ and the temperature field is prescribed by

$$T(x, z) = T_0 e^{\lambda_1 x + \lambda_3 (z + h/2)}. \tag{87}$$

We choose $E_0 = 1$, while β_0 is defined by $\beta_0 T_0 = \frac{10^{-4} E_0}{1-\nu}$. A clamped-clamped situation is analyzed. This example is solved analytically by Lü et al. [29] based on a two-dimensional thermo-elastic model. Lezgy-Nazargah [30] analyzed the same problem using a fully coupled isogeometric two-dimensional finite element approach. For sake of comparison we consider an ANSYS solution with a very fine mesh (1000x100) of fully integrated quadrilateral plane stress elements. A study of the transverse displacements is depicted in Fig. 11. We observe a close agreement of the evaluated bending line compared to ANSYS (Fig. 11(a)). A convergence study with respect to the number of elements over the length N and thickness n is given in Fig. 11(b), indicating a fast rate of convergence. For $N = n \geq 6$ a relative error of less than $\pm 3\%$ is provided, while the present approach converges to a 3% stiffer solution compared to ANSYS. In Fig. 12 the stress distributions at $x = L/2$ are compared to ANSYS and to the solutions published in [29, 30]. The axial thermal stress distribution σ_{xx} is in good agreement compared to the reference solutions (see Fig. 12(a)). The transverse shear stress distributions τ_{xz} are less accurate (see Fig. 12(b)). Considering the maximum shear the analytical solutions of Lü et al. are in good agreement to ANSYS, Lezgy-Nazargah's results show a relative error of 13%, while our proposed algorithm delivers a relative error of 10%. A qualitative comparison indicates that our peak stress is located at $z = 0.0018$ (neutral plane) while the continuum solutions show a

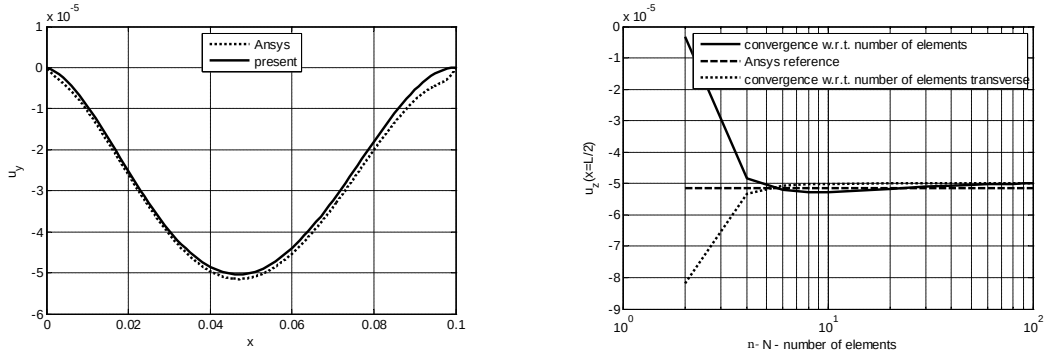

(a) Comparison of transverse displacement $u_z(x)$ with $N = n = 100$

(b) Convergence study of transverse displacement $u_z(x = {}^{L}/_{2})$ with respect to number of shell elements N ($n = 100$) and discretization in transverse direction n ($N = 100$)

Figure 11: Transverse displacement of bi-directional thermo-elastic beam

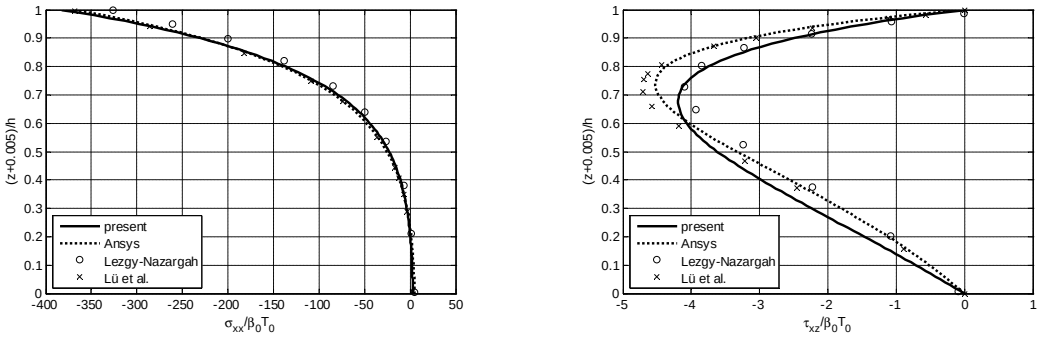

(a) Axial stress distribution

(b) Shear stress distribution

Figure 12: Stress analysis of bi-directional thermo-elastic beam at $x = {}^{L}/_{2}$ with $N = n = 100$ subjected to a non-uniform temperature field

peak-location of $z = 0.0023$. This may stem from stress rearrangements in the two-dimensional regime which are not covered in our proposed approach.

3.3 FGM shell structure

Consider a hemisphere with a radius $R = 10$ and a thickness of $h = 0.5$ (Fig. 13(a)). Due to symmetry only one quarter of the structure is discretized by a mesh according to Fig. 13(b). The material properties and boundary conditions depend only on the radial coordinate r, thus, only one quarter of the structure needs to be analyzed[3]. The model is loaded at the inner and outer surface with a convection boundary condition,

$$h_{ct} = h_{cb} = 10 \ , \ \ T_{Bt} = 0 \ , \ \ T_{Bb} = 300. \tag{88}$$

At the equator the mean temperature is kept at $\overline{T} = 500$. Due to these thermal boundary conditions we expect strong variations of temperature in thickness direction $\hat{z}$ and in membrane

[3]This axisymmetric problem could be analyzed with less than a quarter, however, in order to check the performance of the proposed formulation regarding warped element configurations, we use on quarter of the structure.

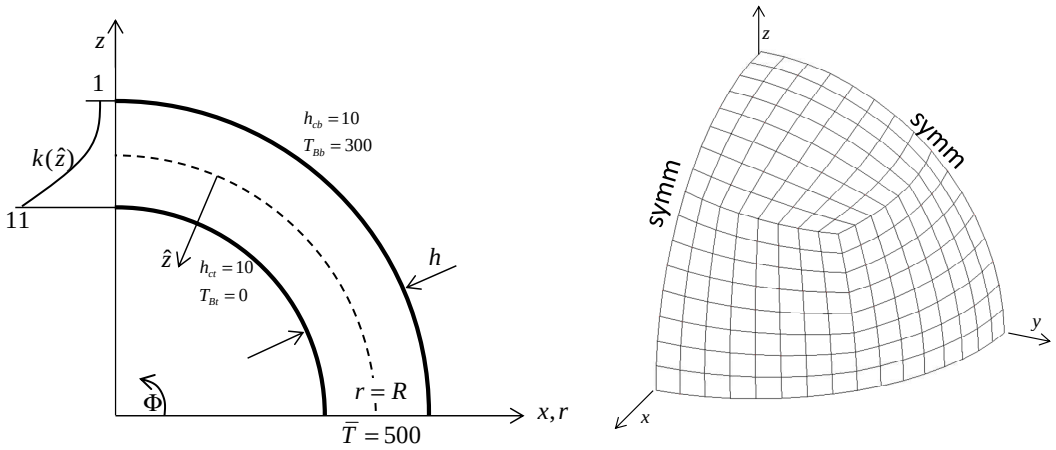

(a) FGM shell structure (b) Shell mesh: $N = 192$

Figure 13: Problem description - FGM shell structure

	u_r	u_z	Error in u_r	Error in u_z
ANSYS	0.2104	-0.1256	-	-
Present $N = 48$ elements	0.2646	-0.1216	25.7%	3.2%
Present $N = 192$ elements	0.2261	-0.1211	7.5%	3.6%
Present $N = 768$ elements	0.2100	-0.1210	0.2%	3.7%

Table 2: Displacements of FGM shell structure

direction ϕ. The material parameters show only spatial variations of the thermal conductivity,

$$k(\hat{z}) = 3.5 + 20\hat{z} + 40\hat{z}^2, \tag{89}$$

representing a parabolic distribution with low conductivity at the outside, $k(\hat{z} = -h/2) = 1$, and high conductivity at the inner surface, $k(\hat{z} = h/2) = 11$. Since we focus mainly on temperature effects Young's modulus E, Poisson's ratio ν and thermal expansion α are assumed constant with respect to the thickness direction, i.e.

$$E = 10 \ , \ \ \nu = 0.3 \ , \ \ \alpha = 1 \cdot 10^{-4}. \tag{90}$$

Elastic solutions of an FGM hemisphere with a varying Young's modulus can be found in [16]. The reference results are evaluated using an axisymmetric model in ANSYS with the fully coupled PLANE 13 element and a very fine discretization of 100×500. For sake of convenience we apply a thermal Dirichlet boundary condition of $T(R - h/2 \leq x \leq R + h/2) = 500$ accepting some error discussed in Sect. 3.1. The temperature distributions with respect to the meridian $0 \leq \phi \leq 90$ are shown in Fig. 14(a). Due to high[4] convection coefficients $h_{cb} = h_{ct} = 10$ the results do not show any variations for $\phi > 20$. The temperature field with respect to the thickness direction is depicted in Fig. 14(b). The distributions evaluated with the present formulation (solid lines) are compared to the ANSYS solutions, indicting a good accuracy. The displacements in radial direction u_r and in height direction u_z are listed in Tab. 2 for different numbers of shell elements. We observe a clear convergence with respect to N for displacements

[4]The term "high" can not be seen absolutely, however, it causes large thermal gradients with respect to the meridian direction ϕ.

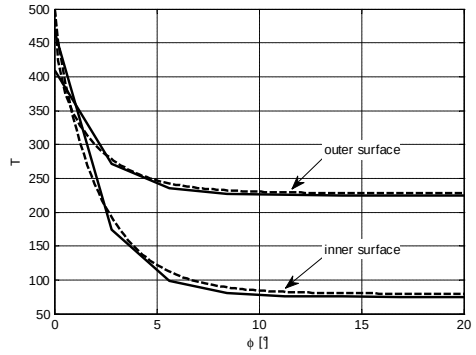

(a) Temperature distribution along the meridian

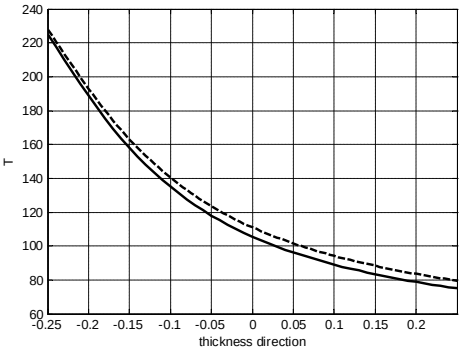

(b) Temperature distribution with respect to $\hat{z}$ at $\phi = 90$

Figure 14: Temperature distributions in FGM shell structure (Solid line: Present formulation, Dashed line: ANSYS) - $N = 768$, $n = 50$, $I = 10$

in radial direction leading to very accurate results for $N = 768$. In terms of displacements in height direction some error of $< 4\%$ has to be accepted. Since a main issue of the proposed

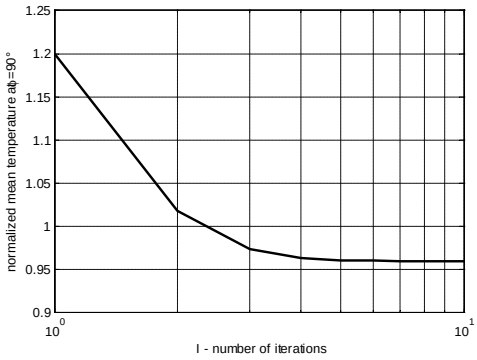

(a) Convergence of $\overline{T}$ at $\phi = 90$ with respect to I

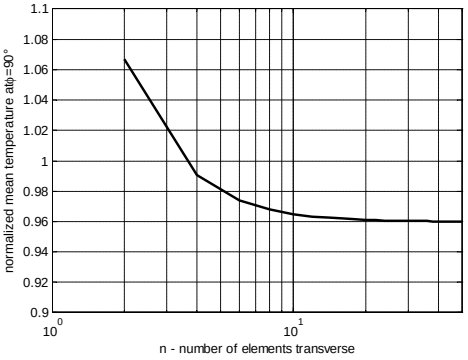

(b) Convergence of $\overline{T}$ at $\phi = 90$ with respect to n

Figure 15: Convergence issues in FGM shell structure

procedure is the iterative strategy discussed on page 5, the convergence of mean temperature $\overline{T}$ (normalized to the ANSYS result) at $\phi = 90$ with respect to the number of iterations I is studied in Fig. 15(a). There, a stable value is reached after six iterations. A final error of less than four percent is also indicated in Fig. 14 and stems from the large temperature gradient in meridian direction at the equator, which may not be resolved properly with low numbers of N. Figure 15(b) indicates convergence with respect to the number of elements discretizing the transverse direction. Obviously, using fifty elements in transverse direction leads to accurate solutions.

4 Conclusion

In this paper a novel approach to the evaluation of thermo-elastic effects in FGM or multi-layer shell structures is proposed. The temperature field is evaluated by an iterative procedure assuming non-constant temperature variations with respect to the thickness direction. A key issue is the decomposition of $T(\hat{x}, \hat{y}, \hat{z})$ according to (11). The resulting displacement fields are evaluated with the aid of a quadrilateral shell element based on effective elastic quantities.

Suitable projection schemes enable an independent derivation of the membrane and the plate bending part. Drilling rotations are included based on an enlarged functional, where the symmetry of stress and strain is enforced only in a weak sense. Special strain field interpolations ensure that all parts of the stiffness matrix can be given analytically even for arbitrarily shaped element configurations, thus, any Gaussian quadrature is avoided. It is shown that thermal expansion causes internal forces and couples, which are applied onto the proposed shell element. The resulting analysis procedure can be termed efficient and leads to accurate results compared to ANSYS solutions where continuum formulations are used.

5 Acknowledgment

This work has been supported by grants of Science and Technology Assistance Agency no. APVV-0246-12 and Scientific Grant Agency of the Ministry of Education of Slovak Republic and the Slovak Academy of Sciences and VEGA No. 1/0453/15.

REFERENCES

[1] B. Abbasnejad, G. Rezazadeh, Mechanical behavior of a fgm micro-beam subjected to a nonlinear electrostatic pressure, International Journal of Materials and Design 8 (2012) 381–392.

[2] B. Sankar, An elasticity solution for functionally graded beams, Composites Science and Technology 61 (2001) 689–696.

[3] S. Chakraborty, S. Gopalakrishnan, J. Reddy, A new beam finite element for the analysis of functionally graded materials, International Journal of Mechanical Sciences 45 (2003) 519–539.

[4] A. Mahi, E. A. Bedia, A. Tounsi, I. Mechab, An analytical method for temperature-dependent free vibration analysis of functionally graded beams with general boundary condition, Composite Structures 92 (2010) 1877–1887.

[5] J. Murin, V. Kutis, Improved mixture rules for the composite (fgm s) sandwich beam finite element, Proceedings IX international conference on compotational plasticity (COMPLAS IX), Barcelona.

[6] J. Murin, V. Kutis, An effective multilayered sandwich beam-link finite element for solution of the electro-thermo-structural problems, Computers & Structures 87 (2009) 1496–1507.

[7] J. Murin, M. Aminbaghai, V. Kutis, Exact solution of the bending vibration problem of fgm beams with variation of material properties, Engineering Structures 32 (2010) 1631–1640.

[8] S. Shen, Functionally graded materials - Nonlinear analysis of shear deformable FGM plates and shells, Taylor and Francis Group, 2009.

[9] K. Liew, X. He, S. Kitipornchai, Finite element method for feedback control of fgm shells in the frequency domain via piezoelectric sensors and actuators, Computer Methods in Applied Mechanics and Engineering 193 (2004) 257–273.

[10] A. Alibeigloo, Static analysis of a functionally graded cylindrical shell with piezoelectric layers as sensor and actuator, Smart Materials and Structures 18 (2009) 12pp.

[11] R. Naghdabadi, S. H. Kordkheili, A finite element formulation for analysis of functionally graded plates and shells, Archive of applied mechanics 74 (2005) 375–386.

[12] S. Kugler, Development of a laterally pressed quadrilateral shell element, Ph.D. thesis, STU Bratislava (2010).

[13] S. Kugler, P. Fotiu, J. Murin, A highly efficient membrane finite element with drilling degrees of freedom, Acta Mechanica 213 (2010) 323–348.

[14] T. J. Hughes, F. Brezzi, On drilling degrees of freedom, Computer Methods in Applied Mechanics and Engineering 72 (1989) 105–121.

[15] S. Kugler, P. Fotiu, J. Murin, The numerical analysis of fgm shells with enhanced finite elements, Engineering Structures 49 (2013) 920–935.

[16] S. Kugler, P. Fotiu, J. Murin, Enhanced functionally graded material shell finite elements, ZAMM Z. Angew. Math. Mech. (2013) 1–13.

[17] O. C. Zienkiewicz, R. L. Taylor, Finite Element Method: Volume 2, Solid Mechanics (Finite Element Method), Butterworth-Heinemann, 2000.

[18] T. Belytschko, W. Liu, B. Moran, Nonlinear Finite Elements for Continua and Structures, Wiley, 2000.

[19] A. Mills, Basic Heat and Mass Transfer, Prentice Hall, 1999.

[20] O. C. Zienkiewicz, R. L. Taylor, Finite Element Method: Volume 1, The Basis (Finite Element Method), Butterworth-Heinemann, 2000.

[21] T. Belytschko, I. Leviathan, Projection schemes for one-point quadrature shell elements, Computer Methods in Applied Mechanics and Engineering 115 (1994) 277–286.

[22] T. Belytschko, I. Leviathan, Physical stabilization of the 4-node shell element with one point quadrature, Computer Methods in Applied Mechanics and Engineering 113 (1994) 321–350.

[23] C. Rankin, B. Nour-Omid, The use of projectors to improve finite element performance, Computers & Structures 30 (1988) 257–267.

[24] S. Kugler, P. Fotiu, J. Murin, Advances in quadrilateral shell elements with drilling degrees of freedom, H. Altenbach and V. Eremeyev (eds.) Shell-like Structures - Advanced Structured Materials Vol. 15 (2011) 307–328.

[25] S. Kugler, P. Fotiu, J. Murin, Thermo-elasticity in shell structures made of functionally graded materials, Acta Mechanica (2016) 10.1007/s00707–015–1550–9.

[26] K. Bathe, E. Dvorkin, A formulation of general shell elements - the use of mixed interpolation of tensorial components, International Journal for Numerical Methods in Engineering 22 (1986) 697–722.

[27] E. Dvorkin, K. Bathe, A continuum mechanics based four-node shell element for general non-linear analysis, Eng. Comput. 1 (1984) 77–88.

[28] ANSYS, Ansys V11 Documentation.

[29] C. Lü, W. Chen, R. Xu, C. Lim, Semi-analytical elasticity solutions for bi-directional functionally graded beams, International Journal of Solids and Structures 45 (2008) 258–275.

[30] M. Lezgy-Nazargah, Fully coupled thermo-mechanical analysis of bi-directional fgm beams using nurbs isogeometric finite element approach, Aerospace Science and Technology 45 (2015) 154–164.